Nuclear Physics B262 (1985) 689-714

MEASUREMENT OF SMALL-ANGLE ANTIPROTON-PROTON AND PROTON-PROTON ELASTIC SCATTERING AT THE CERN INTERSECTING STORAGE RINGS

N. AMOS[a], M.M. BLOCK[a], G.J. BOBBINK[b],[i], M. BOTJE[c], D. FAVART[d], C. LEROY[d],[ii], F. LINDE[c], P. LIPNIK[d], J-P. MATHEYS[d],[iii], D. MILLER[a], K. POTTER[b], S. SHUKLA[a], C. VANDER VELDE-WILQUET[b],[iv] and S. ZUCCHELLI[a]

Received 14 June 1985

Antiproton-proton and proton-proton small-angle elastic scattering was measured for centre-of-mass energies $\sqrt{s} = 30.6$, 52.8 and 62.3 GeV at the CERN Intersecting Storage Rings. In addition, proton-proton elastic scattering was measured at $\sqrt{s} = 23.5$ GeV. Using the optical theorem, total cross sections are obtained with an accuracy of about 0.5% for proton-proton scattering and about 1% for antiproton-proton scattering. The measurement of the interference of the Coulomb scattering and the hadronic scattering permits a determination of the ratio of the real-to-imaginary part of the forward hadronic scattering amplitude. Also presented are measurements of the hadronic slope parameter.

1. Introduction

The proton-proton total cross section, $\sigma_{\text{tot}}(\text{pp})$, has been shown to rise over the energy range of the CERN Intersecting Storage Rings (ISR) in two experiments, performed independently by the CERN-Rome Collaboration (CR) [1] and the Pisa-Stony Brook Collaboration (PSB) [2]. These two experiments used different methods: the PSB group directly measured the total interaction rate while in the CR experiment the total cross sections were deduced, via the optical theorem, from the elastic scattering in the forward region. Extending their measurements of the pp differential cross sections through the region of Coulomb-hadronic interference, the CR Collaboration also extracted the ratio of the real to the imaginary part of the forward hadronic scattering amplitude, $\rho(\text{pp})$ [3, 4].

The construction of the Antiproton Accumulator and the subsequent operation of the ISR as an antiproton-proton collicer offered the possibility to extend these measurements to $\bar{\text{p}}\text{p}$ scattering. Our experiment is dedicated to the measurement of

[a] Northwestern University, Evanston, Illinois, USA.
[b] CERN, Geneva, Switzerland.
[c] State University, Utrecht, The Netherlands.
[d] Université Catholique de Louvain-la-Neuve, Belgium.
[i] Now at Physics Department, Carnegie-Mellon University, Pittsburgh, USA.
[ii] Now at Physics Department, McGill University, Montreal, PQ, Canada.
[ii] Now at Physics Department, Hua-Zhong Normal University, Wuhan, China.
[iv] Now at IIHE, Université Libre de Bruxelles, Belgium.

$\bar{p}p$ and pp small-angle elastic scattering using the method pioneered by the CR-Collaboration. In previous letters [5] we have reported $\bar{p}p$ and pp results obtained at the centre-of-mass energies $\sqrt{s} = 30.7$, 52.8 and 62.5 GeV. Using the optical theorem, a fit to the differential elastic cross sections enabled us to determine the $\bar{p}p$ total cross-section which was found rising over the ISR energy range. The same conclusion was reached by Carboni et al. [6] from their measurement of the $\bar{p}p$ total interaction rate at $\sqrt{s} = 52.8$ GeV. In addition, our measurement at $\sqrt{s} = 30.7$ and 52.8 GeV of the Coulomb scattering and its interference with the hadronic scattering allowed a determination of ρ. Our results have demonstrated that $\rho(\bar{p}p)$ is positive and rising over the ISR energy range. The large positive values we observe for $\rho(\bar{p}p)$ and $\rho(pp)$ indicate that the $\bar{p}p$ and pp total cross section should continue to rise beyond ISR energies. Indeed, recent measurements of $\sigma_{tot}(\bar{p}p)$ at the CERN SPS Collider [7, 8] have shown that this rise continues up to $\sqrt{s} = 540$ GeV.

The aim of the present paper is to report the final analysis of our measurements. It is organized as follows: The method of our measurements is described in sect. 2. A description of the apparatus and details about the information recorded are given in sect. 3. The operations of the experiment are described in sect. 4. Details about the luminosity measurement are presented in sect. 5. Sect. 6 is devoted to the data reduction. The analysis is described in sect. 7. Finally, the results are discussed in sect. 8.

2. Method

The experimental method consists in measuring the $\bar{p}p$ and pp differential elastic cross section, $d\sigma/d|t|$, at small four-momentum transfer squared, typically $0.5 \times 10^{-3} < |t| < 50 \times 10^{-3}$ GeV^2.

The differential elastic cross section is

$$d\sigma/d|t| = \pi |f_h(s, t) + f_c(s, t)|^2 , \tag{1}$$

with f_h (f_c) the hadronic (Coulomb) amplitude.

At small momentum transfer, the hadronic amplitude is parametrized as

$$f_h(s, t) = f_h(s, 0)\, e^{-b|t|/2} = (1/4\pi)\sigma_{tot}(\rho + i)\, e^{-b|t|/2} , \tag{2}$$

with b the hadronic slope parameter and ρ the ratio of the real-to-imaginary part of f_h. In eq. (2) the usual assumption is made that ρ is independent of t. The total cross section, σ_{tot}, is introduced through the optical theorem:

$$\sigma_{tot} = 4\pi \, \mathrm{Im} \, f_h(s, 0) . \tag{3}$$

The proton-proton Coulomb amplitude is parametrized as

$$f_c(s, t) = -2\alpha G^2(t)\, e^{i\alpha\phi}/|t| . \tag{4}$$

Here α is the fine structure constant, $G(t)$ the usual proton electromagnetic form factor

$$G(t) = [1 + |t|/(0.71\ \mathrm{GeV}^2)]^{-2} \tag{5}$$

and ϕ the Coulomb-hadronic phase. This phase, originally calculated by Bethe [9], is essentially reproduced by a calculation of West and Yennie [10], whose expression we use:

$$\phi = \ln(0.08\ \mathrm{GeV}^2/|t|) - 0.577\,. \tag{6}$$

A recent calculation by Cahn [11] gives a result which is close to that of West and Yennie.

Combining eqs. (1)-(4) the pp differential elastic cross section can be written as follows, for $\alpha\phi \ll 1$:

$$\begin{aligned} \mathrm{d}\sigma/\mathrm{d}|t| = {} & 4\pi\alpha^2 G^4(t)/|t|^2 - \sigma_{\mathrm{tot}}\alpha(\rho + \alpha\phi)G^2(t)\,\mathrm{e}^{-b|t|/2}/|t| \\ & + (1+\rho^2)\sigma_{\mathrm{tot}}^2\,\mathrm{e}^{-b|t|}/(16\pi)\,. \end{aligned} \tag{7}$$

The same expression applies to $\bar{p}p$ elastic scattering, provided a change of sign of α is made in eq. (7). The three terms in eq. (7), describe the Coulomb, the Coulomb-hadronic intereference and the hadronic contribution to $\mathrm{d}\sigma/\mathrm{d}|t|$ respectively. The interference is largest at $|t| \cong 8\pi\alpha/\sigma_{\mathrm{tot}} \approx 2\times 10^{-3}\ \mathrm{GeV}^2$, where the Coulomb and hadronic contributions are equal in magnitude. By integrating the hadronic term over $|t|$, the total elastic cross section is obtained:

$$\sigma_{\mathrm{el}} = (1+\rho^2)\sigma_{\mathrm{tot}}^2/(16\pi b)\,. \tag{8}$$

In this experiment, the parameters σ_{tot}, ρ and b are extracted from a fit of eq. (7) to the measured differential cross sections. With this method, the determination of the absolute scale of σ_{tot} depends on the square root of the measured luminosity. The measurement of the Coulomb scattering, the t-dependence of which is known, permits a calibration of the t-scale.

3. Apparatus

The layout of the experiment is shown in fig. 1. The detector consisted of eight scintillator hodosocopes. Four of these, the "internal" hodoscopes, were placed symmetrically above and below the ISR vacuum chamber inside thin walled (0.2 mm stainless steel) movable indents ("roman pots") at a distance of 8.7 m from the intersection region. These hodoscopes could be positioned under remote control with an accuracy of about 0.02 mm. Each internal hodoscope consisted of 24 horizontal "stack" counters, 2 mm high, to measure polar scattering angles and 7 vertical "finger" counters, 4 mm wide, to measure azimuthal angles. The area of stacks and fingers was covered by a single trigger counter. The height (width) of the stack (finger) counters was machined to an accuracy of 5 μm. A circular beam

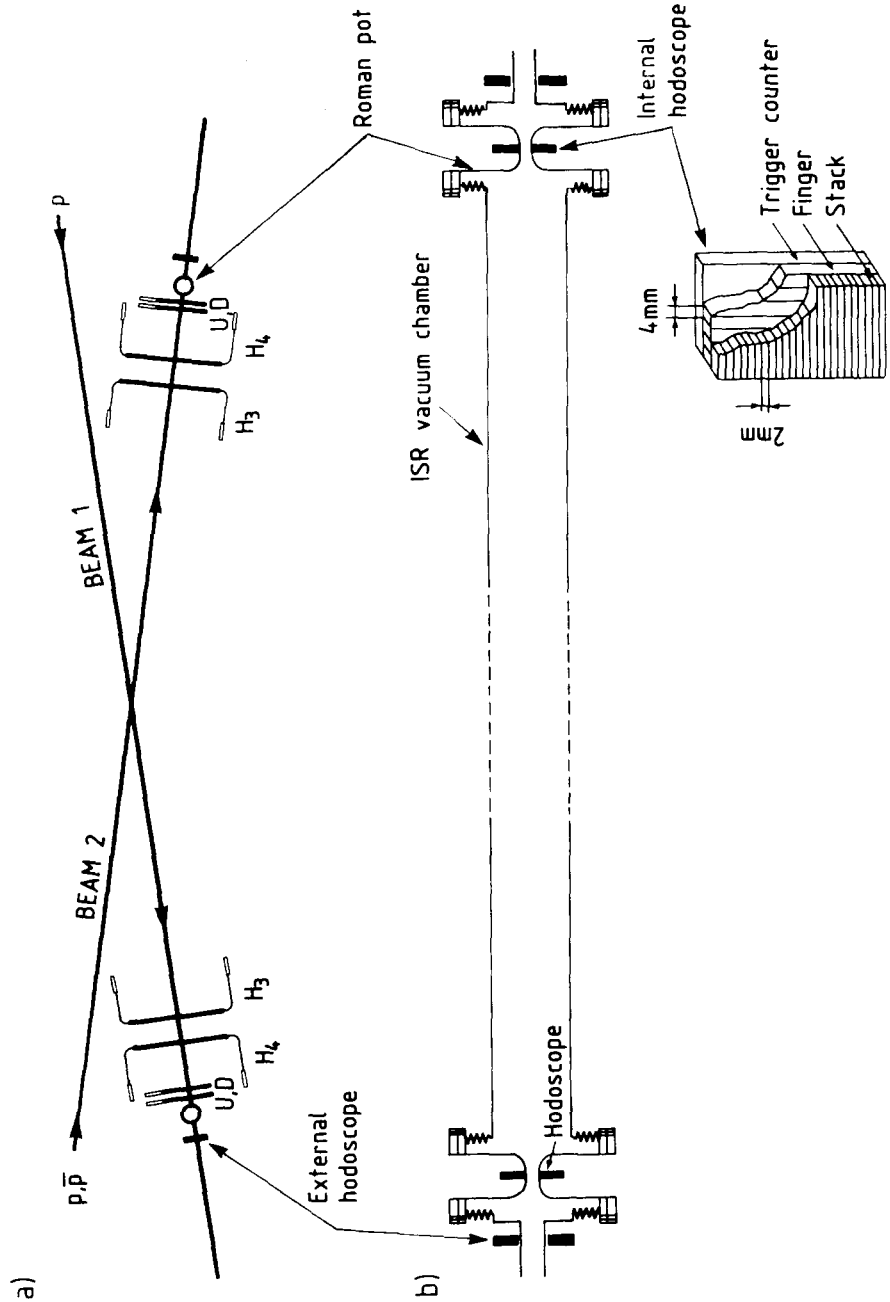

Fig. 1. Top view (a) and side view (b) of the intersection region showing the location of the "roman pots", the scintillation counter hodoscopes and the scintillation counter telescopes used for the luminosity measurement.

pipe with a diameter of 17 cm allowed particles which were scattered at angles of less than 10 mrad to travel free from obstructions and reach the internal detectors after traversing only the thin wall of the roman pot.

The other four hodoscopes were placed at fixed positions behind the internal hodoscopes at 9.0 m from the intersection. These "external" hodoscopes consisted of two separate units each. One unit was an assembly of 12 stack counters, 4.5 mm high. The other unit, placed directly behind the plane of stacks consisted of 11 finger counters, 8 mm wide. The height of the stacks and the width of the fingers were machined to an accuracy of about 20 μm. Each detector plane was subtended by a trigger counter. The external hodoscopes covered a range in polar angle $4 < \vartheta < 11$ mrad. These hodoscopes provided us with independent checks on the efficiency of the internal hodoscopes.

In addition, several combinations of large scintillation counters were used for luminosity measurement. Four telescopes, U_1, U_2, D_1 and D_2, each made of two scintillation counters (100×50 cm^2), were located symmetrically above (U) and below (D) the beam pipes at 8.4 m downstream from the intersection region. Two independent monitors were formed by the coincidences U_1U_2 and D_1D_2. Furthermore, we used a monitor (H_3H_4), which was made of the coincidence of four large circular arrays (1.8 m in diameter) positioned around the downstream vacuum chambers at 6.7 m from the intersection. The signals of H_3H_4 were kindly provided to us by the CERN-Naples-Pisa-Stony Brook Collaboration [6].

A coincidence of the signal from the trigger counter of the internal hodoscope located above (below) one beam and the signal from the trigger counter of the internal hodoscope located below (above) the other beam were used to trigger the recording of elastic events. Similar coincidences triggered the recording of elastic events in the external hodoscopes. When a trigger occurred, the system was inhibited and the pulse heights of the internal and the external hodoscope counters were recorded. These pulse heights and the time-of-flight (TOF) differences measured between the various pairs of trigger counter signals were written to magnetic tape. Between triggers, the luminosity coincidences were accumulated in scalars and time-of-flight differences between the various combinations of luminosity counters were measured. A high-frequency clock kept track of the total active time. The data acquisition was controlled by a PDP-11/34 on-line computer.

4. Data taking

The data presented here were taken in the period August 1981–June 1982. They include three $\bar{p}p$ runs taken at $\sqrt{s} = 52.6$, 62.3 and 30.4 GeV where we collected 170 000, 120 000 and 59 000 elastic $\bar{p}p$ events respectively. Proton-proton comparison data were taken at the same energies in a series of short runs of one to two days each, immediately before or after the $\bar{p}p$ runs. In addition, pp elastic scattering was measured at $\sqrt{s} = 23.5$ GeV. Two to three million pp elastic events were collected

TABLE 1
Running conditions

ISR run	Type	Running time (h)	$\sqrt{s}$ (GeV)	I(p) (A)	I(p/$\bar{p}$) (A)	L ($cm^{-2}\,s^{-1}$)	Elastic events $\times 10^5$
1209	pp	26	23.5	3.3	3.4	2×10^{29}	6.1
1223	pp	20	52.8	3.3	3.4	4×10^{29}	9.6
1225	pp	25	52.8	4.4	4.8	6×10^{29}	17.8
1226	pp	18	23.5	2.2	2.5	1×10^{29}	5.8
1229	$\bar{p}p$	246	52.6	8.8	1.9×10^{-3}	5×10^{26}	1.7
1252	pp	30	62.3	5.0	5.0	6×10^{29}	14.0
1257	$\bar{p}p$	109	62.3	10.0	3.2×10^{-3}	8×10^{26}	1.2
1271	pp	27	30.6	6.0	6.0	8×10^{29}	16.4
1272	$\bar{p}p$	225	30.4	8.4	4.1×10^{-3}	9×10^{26}	0.6
1274	pp	39	30.6	5.2	5.3	5×10^{29}	13.0

at each energy. The running conditions are summarized in table 1. Details on the performance of the CERN antiproton facility and the ISR can be found in refs. [12] and [13].

This experiment required special beam conditions. As our apparatus had no capability of vertex reconstruction, but relied on the collinearity of the two scattered particles as the signature of elastic events, it was important that the spatial extent of the interaction region (diamond) be as small as possible. This was achieved by: (i) operating the ISR in the Terwilliger mode [14] to obtain zero-momentum dispersion at the interaction point; (ii) optimizing injection and subsequent beam scraping to select only those particles injected with the smallest betatron oscillation amplitudes; (iii) careful machine tuning to stay well away from all low-order coupling resonances and (iv) minimizing the coupling between the vertical and horizontal betatron motion using the skew quadrupole correction scheme. As a result, the length of the interaction diamond was reduced from ~40 cm to ~4 cm while the vertical dimension was kept as small as possible.

During part of the run, the detectors were operated close to the circulating beams, corresponding to an angular coverage of typically $1 < \vartheta < 6$ mrad. The horizontal diamond position with respect to the detector was deduced from measurements of the azimuthal distribution of elastic events and the beams were subsequently steered radially to bring them on the centre line of the apparatus. In general, data were also taken with the detectors in a retracted position (typically $3 < \vartheta < 8$ mrad) in order to extend the t-range covered by the measurements. The single rates in the detector were kept at an acceptable level by placing a series of collimators close to the beam and with regular scraping to remove the particles in the halo. In this way, good running conditions were obtained with the first detector element as close as ~8 mm to circulating beams of about 10 A. The data collected in both the $\bar{p}p$ and the pp runs were essentially free from background.

5. Luminosity measurement

The differential elastic cross sections are determined from the measurement of the t-dependence of the elastic interaction rate, normalized to the machine luminosity:

$$d\sigma^{meas}/d|t| = (R^{el}/\Delta\Omega)(\pi/p^2)(1/L), \tag{9}$$

where R^{el} is the elastic counting rate recorded in the solid angle $\Delta\Omega$, p the beam momentum and L the luminosity. The counting rate of the monitor (R_M), the monitor constant (σ_M) and the luminosity are related through

$$R_M = \sigma_M L. \tag{10}$$

The luminosity monitor system is described in sect. 2. For pp, we used the two independent luminosity monitors formed by the U_1U_2, D_1D_2 coincidences and the large H_3H_4 counters. For the $\bar{p}p$ runs it was necessary to use in addition a monitor formed by the combination $(U_2+D_2)H_3H_4$, called MONI in the following. The geometry of the U_1U_2, D_1D_2 and MONI monitors was efficient in rejecting the relatively high background in $\bar{p}p$ runs arising from the high-current proton beam.

The luminosity monitor constants were determined with the van der Meer method [15] in special runs interleaved with data taking. For each ISR run, up to three calibration runs were taken. During these runs, the beams were displaced vertically with respect to each other in small accurate steps. The monitor counting rate R_M was measured as a function of the beam separation λ and the luminosity monitor constant calculated from:

$$\sigma_M = C(I_1 I_2)^{-1} \int R_M(\lambda)\, d\lambda. \tag{11}$$

Here I_1 and I_2 are the beam currents and the constant of proportionality is $C = 0.9975 \times 10^{-28}$ cm s A^2 at the ISR.

At each displacement, the beam currents, the counting rates and the TOF differences were measured for the various luminosity counter coincidences. The observed TOF distribution of luminosity events (see fig. 2) has two components: a narrow peak centered at zero time difference, coming from beam-beam events and a continuous background contribution from interaction of one of the beams with the residual gas or vacuum chamber walls, upstream from the interaction region. Correction for background under the beam-beam peak was done by extrapolation of the background observed in two TOF windows on either side of the peak. The luminosity monitor constant, σ_M, was computed from eq. (11) by numerical integration of a multi-parameter interpolation function fitted to the counting rates measured at the various beam displacements (see fig. 3).

The accuracy of such a calibration was typically 0.8% and was always better than 1%. For the $\bar{p}p$ run at $\sqrt{s} = 30.4$ GeV it was about 2.5%, due to higher background conditions. This includes the statistical error, uncertainties induced by the analysis

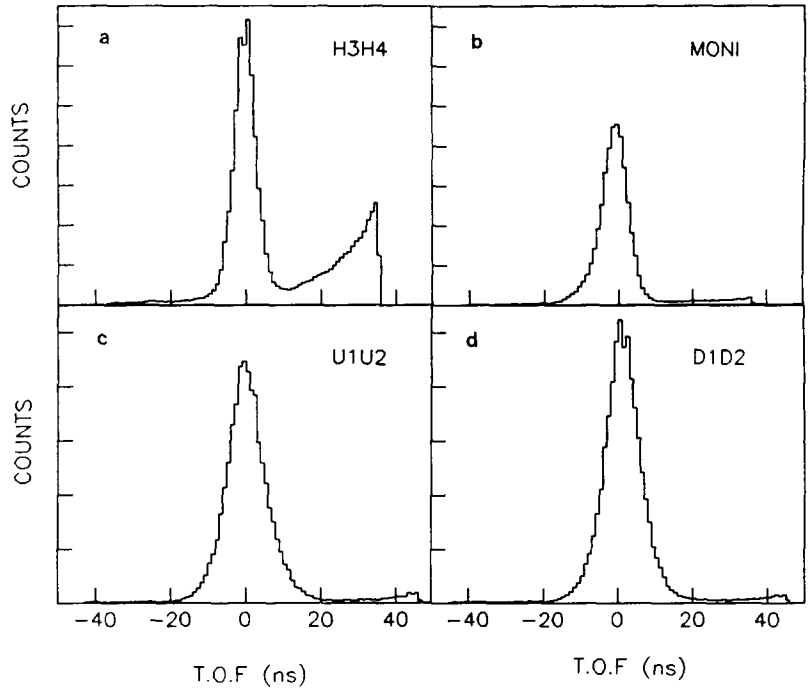

Fig. 2. Time-of-flight spectra for the various luminosity monitors recorded during a $\bar{p}p$ run: (a) H_3H_4, (b) MONI, (c) U_1U_2, (d) D_1D_2. Beam-beam events are accumulated in the peak. The background arising from the high current proton beam is strongly suppressed in the monitors MONI, U_1U_2 and D_1D_2.

procedure and external consistency errors inferred from comparison of consecutive calibrations within one ISR run.

Not included is the error on the beam displacement scale which contributes like $\Delta\sigma_M/\sigma_M = \Delta\lambda/\lambda$. Measures were taken to reduce this contribution: (i) the beams were steered only in our intersection to eliminate disturbance from displacements at other intersections; (ii) the hysteresis in the steering dipoles was taken into account; (iii) dipoles of the adjacent intersections were used as correction elements and (iv) the beams were steered far apart at the beginning of each run and then swept through each other, always moving in one direction. The beam displacements, as determined from magnetic field calculations, were calibrated to an accuracy of $\Delta\lambda/\lambda = 0.4\%$, using a system of beam scrapers driven by precision screws [16].

6. Data reduction

The data reduction and analysis procedures have been described in detail elsewhere [17] and will only be outlined below. To be retained as an elastic scattering candidate, a recorded event had to satisfy the following criteria: (i) the TOF

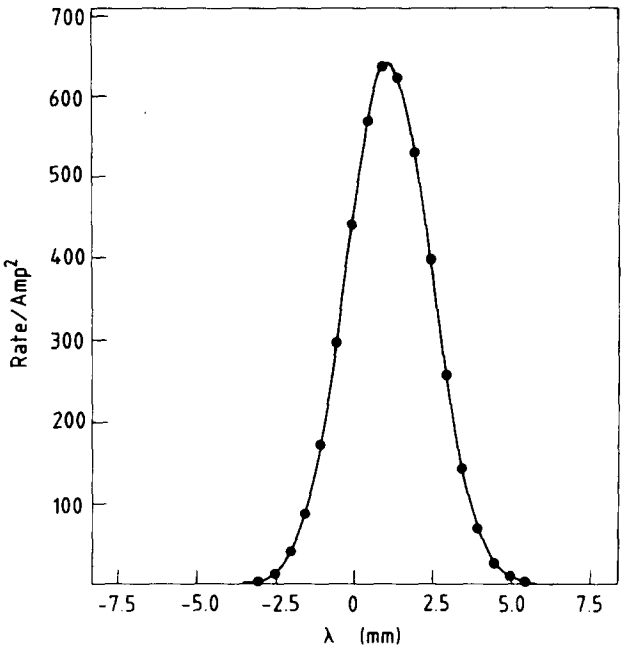

Fig. 3. Luminosity monitor counting rate (normalized to the beam currents) versus beam displacement, measured during a pp van der Meer scan at $\sqrt{s} = 52.8$ GeV. The interpolation curve shown is used to estimate the area under the measurements.

difference of the trigger counters is inside a preset window; (ii) at least one counter in each stack and finger plane of both arms has fired, i.e. a pulse above a preset threshold is recorded; (iii) there is no hit in the monitor H_3H_4, which would identify the event as inelastic.

Elastic scattering candidates were accumulated in a $24\times7\times24\times7$ four dimensional matrix $N(i, j; k, l)$ according to the stack counter (i) and finger counter (j) in arm 1 and stack counter (k) and finger counter (l) in arm 2 they were assigned to. This assignment was straightforward for those events where only one counter had fired in any given plane. However, multiple hits were often observed in one or more planes, either because the event was inelastic and more than one particle had hit the detector, or because of δ-ray production in the counter itself or in the surrounding material. These multiple hit ambiguities were resolved and the corresponding events were assigned as follows: if two hits were recorded in adjacent elements of a given plane, the event was assigned to the counter with the higher pulse; if three hits were recorded in adjacent elements, the event was assigned to the central counter, provided it had the highest pulse; if other multiple hit configurations were encountered in any stack or finger plane of both arms, the event was rejected. The sensitivity of the results to alternative assignment algorithms has been

extensively explored*. No significant differences were observed [17]. Corrections were applied to the matrices $N(i, j; k, l)$ to account for:

(i) The loss of events with pulses below the thresholds set for each counter. These corrections, applied to each stack and finger element separately, were about 0.7% per counter.

(ii) Out-of-time background, as observed in present TOF background windows on either side of the beam-beam peak. The background was extrapolated and subtracted from the number of events observed in preset in-time windows. The corrections were determined for each combination of stack counters in arm 1 and arm 2 separately. They were in general $<1\%$ for the stack counters closest to the beam and negligible for the others.

(iii) Inelastic contamination, as observed in the region of $N(i, j; k, l)$ where the acceptance for elastic events is negligible. The average population of this region was substracted, bin by bin, from the events accumulated in $N(i, j; k, l)$. This correction was typically about 1% in each pair of hodoscopes.

(iv) Losses due to the improper rejection of elastic events by the assignment criteria. To determine these losses, elastic events were identified with the aid of the external hodoscopes. The correction was obtained as the fraction of these events which were rejected by the assignment criteria in the internal hodoscopes. Per pair of hodoscopes, about 2.3% of the elastic events were rejected. The loss remained constant within 0.2% from run to run.

(v) Loss of events caused by the hardware discriminator thresholds on the trigger counter signals. These losses were negligible ($<0.2\%$) for all analysed runs except pp and $\bar{p}p$ taken at $\sqrt{s} = 62.3$ GeV, where some discriminator thresholds were accidentally set above their optimal values. In these runs the losses depend on the scattering angle, due to the non-uniform light collection in the trigger counter. They were about 3-6% in the region close to the beam and decreased to zero towards the larger scattering angles. The corrections for these efficiencies were evaluated by several independent methods [17] which agreed within 1-2%.

Corrections to account for deadspace between counters, improper inelastic rejection by the monitor H_3H_4, events assigned to the wrong counter etc. were all negligible ($<0.1\%$).

The uncertainties in the corrections described above, are either added to the statistical error or added to the error on the normalization of the data (see subsect. 7.1).

7. Analysis

The analysis of the data proceeds in two stages. First, sets of differential elastic cross sections are extracted from the reduced data, properly normalized to the

* Among the possibilities investigated were (i) assignment of double hits weighted by the distribution of single hits and (ii) random assignment of double hits among the counters involved.

measured integrated luminosity. In the second stage, eq. (7) is fitted to the various sets of differential cross sections and the relevant parameters are determined from this fit. Which parameters are extracted from a particular set, depends on the t-range covered by the data. The total cross section could be determined at all energies. The data at the highest energy ($\sqrt{s} = 62.3$ GeV) covered only part of the interference region and were not fitted for ρ. The data at $\sqrt{s} = 23.5$ and 30.6 GeV did not extend to large enough $|t|$ to allow for a reliable measurement of the hadronic slope parameter.

7.1. DETERMINATION OF THE DIFFERENTIAL CROSS SECTIONS

The differential elastic cross-sections were obtained from the measured distributions $N(i, j; k, l)$ as follows. First, an expression is derived which describes the event distribution in a pair of hodoscopes. For this purpose, an elastic event is specified by nine coordinates: three spatial coordinates describing the location of the interaction point, the four initial betatron angles of the incoming particles (all summarized in the 7-dimensional vector X) and the two scattering angles ϑ and φ. The number of particles, originating in the volume element d^7X and scattered into the solid angle $\mathrm{d}\Omega = \mathrm{d}\cos(\vartheta)\,\mathrm{d}\varphi$ is then given by

$$\mathrm{d}n = \mathscr{L} P(X)\,\mathrm{d}\sigma/\mathrm{d}\Omega\,(\vartheta)\,\mathrm{d}^7X\,\mathrm{d}\Omega\,, \tag{12}$$

where $\mathscr{L}$ is the integrated luminosity, $P(X)$ the diamond density distribution, normalized to unity, and $\mathrm{d}\sigma/\mathrm{d}\Omega$ the differential elastic cross section. The distribution of events in a pair of hodoscopes is obtained by integration of eq. (12) over the volume which is seen by two given impact points on the detector. Further integration of this distribution over the dimensions of the cell defined by the overlap of the stack element (i), finger element (j) in arm 1 and the stack element (k), finger element (l) in arm 2, yields a description of the population in the matrix $N(i, j; k, l)$. $P(X)$ was parametrized as a gaussian distribution in the seven coordinates (X) and $\mathrm{d}\sigma/\mathrm{d}\Omega$ is given by eq. (7). With the chosen parametrization and expansion of the expression for $\mathrm{d}\sigma/\mathrm{d}\Omega$ in a Taylor series, the nine-dimensional integration was performed analytically and reduced to well-known error function integrals [18].

In fig. 4 is shown the event distribution in a matrix $N(i, j; k, l)$ after summing over the finger indices (j) and (l). The collinearity of elastic events causes them to be accumulated on the diagonal. The strong variation in population along the ridge, reflects the angular dependence of the differential elastic cross section. The distribution viewed along a coordinate perpendicular to the ridge, i.e. at fixed scattering angle, is essentially a projection of the diamond distribution. The positions and widths of the diamond profiles, which enter into the calculation described above, were obtained from a fit of such projections.

Next, the calculated distribution is used to correct the measured distribution, $N(i, j; k, l)$, for border losses and binning effects. The corrected populations are summed over those combinations of indices i, j, k and l which correspond to a

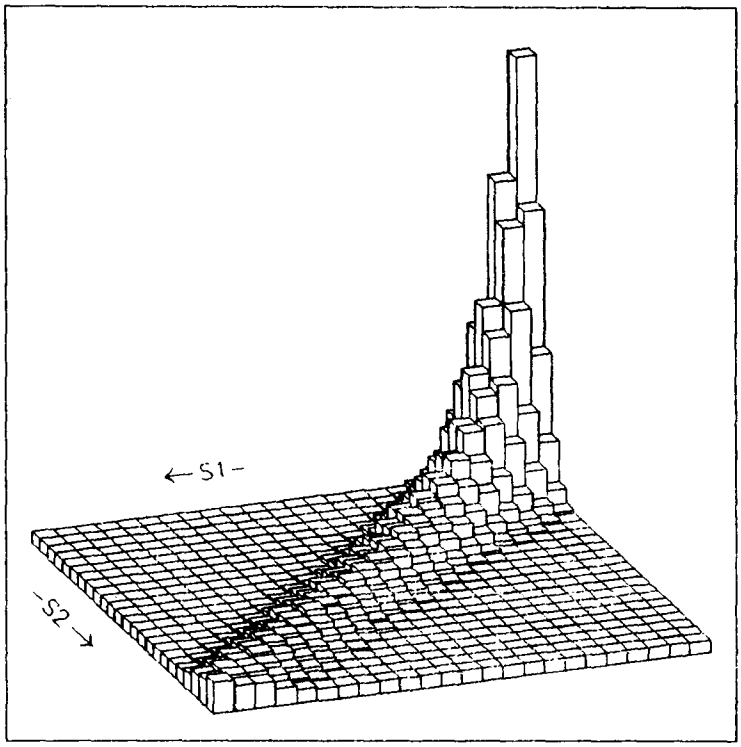

Fig. 4. Collinearity plot of elastic events from a pp run at $\sqrt{s} = 23.5$ GeV. The stack indices S_1 and S_2 run towards larger scattering angles. The angular dependence of the differential elastic cross-section is measured along the ridge and the profile of the beam overlap is measured perpendicular to the ridge.

given scattering angle. Normalization to the integrated luminosity and the covered solid angle, then yields a measurement of $d\sigma/d\Omega$ for each scattering angle defined by the elements of a detector pair.

These angles depend on the location of the stack and finger elements and on the horizontal diamond position with respect to the hodoscopes. The dependence on the latter was removed by scaling the cross sections to sets of nominal scattering angles, which depend on the detector position only, and subsequent averaging. This procedure exploits the left/right symmetry in each detector pair and thus reduces the sensitivity of the cross-section evaluation to the exact diamond position. Further averaging of cross sections obtained from the two detector pairs, exploits the up/down symmetry of the apparatus and reduces the sensitivity to the exact hodoscope position.

The binning corrections are significant (<5%) only in the Coulomb region where the variation of the cross-section with the scattering angle is strongly non-linear. The corrections applied to account for border losses are small: 95–100% of the events were accepted in all regions of the detector except in the edge counters where about 60% of the events were accepted.

An uncertainty of 0.3% on the efficiency calculations, 0.8% (average) on the luminosity monitor constants, 0.4% on the beam displacement scale and the error in the calculation of the integrated luminosity contribute to an error of 1.0% per ISR run on the normalization of the data. For the $\bar{p}p$ run at 30.4 GeV a larger error of 2.5% on the normalization was due to high background conditions.

The analysis procedure described above is essentially iterative, because previous measurements or estimates of σ_{tot}, ρ, and b are used to describe the angular dependence of $d\sigma/d\Omega$ in eq. (12). However, the calculated differential cross sections depend weakly on these parameters since each cell covers a very small range in ϑ and the procedure converges at the first iteration. We verified that the cross section evaluation did not introduce any significant bias by extensive analysis of Monte Carlo generated data.

The measured $\bar{p}p$ and pp differential elastic cross sections are given in tables 2 and 3 and are shown in figs. 5 and 6.

7.2. DETERMINATION OF σ_{tot}, ρ, AND b

Eq. (7) is fitted to the differential elastic cross sections to extract σ_{tot}, ρ, and b. Excluded from all fits were cross section points with an acceptance correction of more than 30%, i.e. those which are evaluated at the edges of the apparatus. Also omitted were data points of $\bar{p}p$ and pp at $\sqrt{s} = 62.3$ GeV for which the trigger counter efficiency corrections were more than 2%.

In addition to the parameters σ_{tot}, ρ and b, a parameter δh is introduced, which is the correction to the average distance between the upper and the lower hodoscopes as measured by optical survey. This parameter provides a calibration of the t-scale and is obtained from the pp data taken at $\sqrt{s} = 23.5$ and 30.6 GeV which extend far into the Coulomb region. The two fitted values of δh are -0.19 ± 0.03 and -0.11 ± 0.02 mm. Although these are marginally compatible, the difference could reflect an accidental change in detector position between these two runs which were separated by a two-month long ISR shut-down. However, it is unlikely that such a change occurred between the runs at $\sqrt{s} = 23.5$ and 52.8 GeV which were taken shortly after each other. The value $\delta h(23.5\ \text{GeV})$ is therefore used in the fit at 52.8 GeV. For the same reason $\delta h(30.6\ \text{GeV})$ is used in the fit at 62.3 GeV. The uncertainty on the t-scale is computed from the distribution of independent determinations of δh which showed an r.m.s. of 0.06 mm.

The pp or $\bar{p}p$ total cross section is a free parameter at all energies. The hadronic slope parameter is obtained from data taken at $\sqrt{s} = 52.8$ and 62.3 GeV which extend far enough into the hadronic region. At other energies published values of $b(pp)$ [19] are taken as input to the fit while $b(\bar{p}p)$ at $\sqrt{s} = 30.4$ GeV is estimated through the following approximate expression deduced from eq. (8):

$$b(\bar{p}p) \approx b(pp) + \Delta\sigma_{tot}(16\pi\sigma_{el}/\sigma_{tot})^{-1}, \tag{13}$$

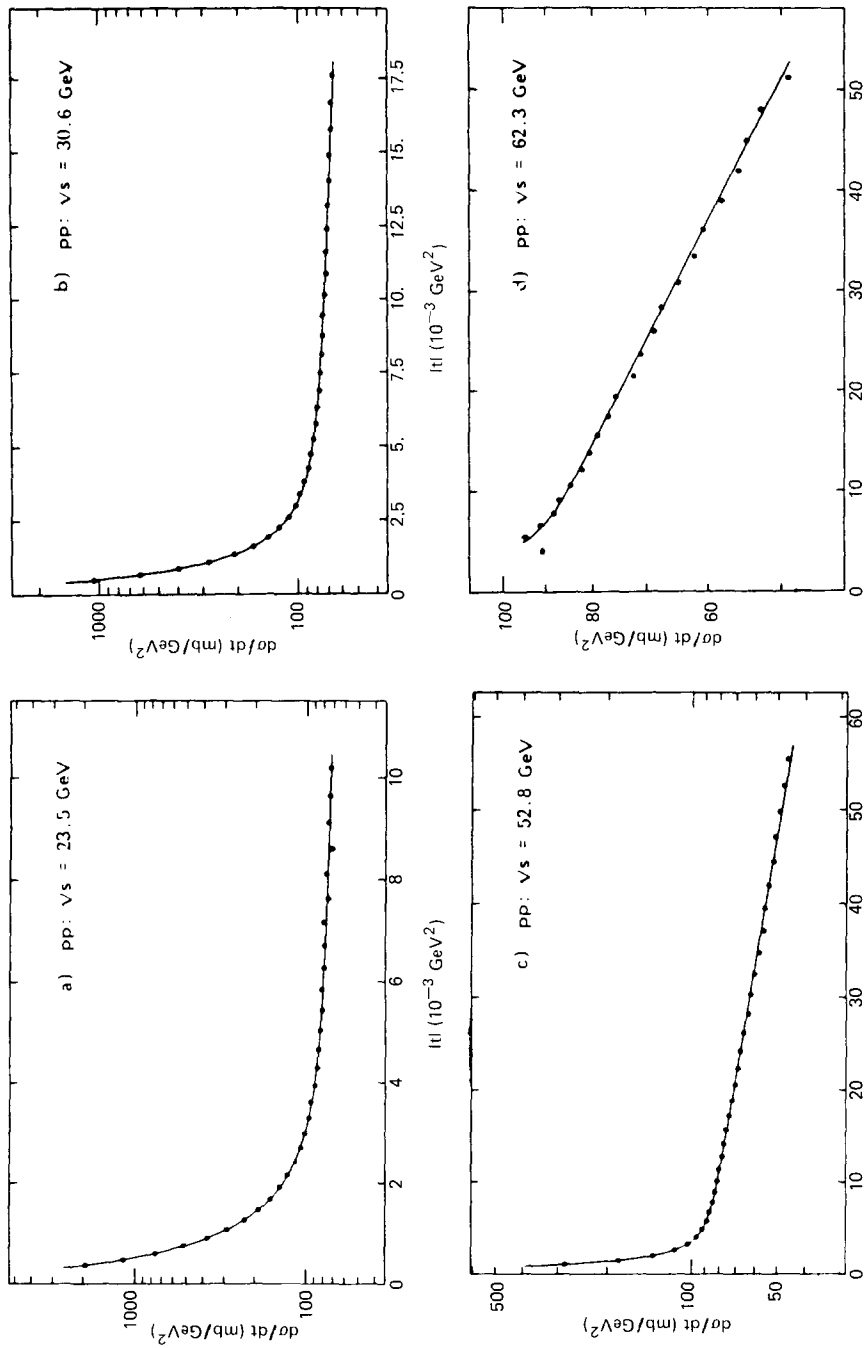

Fig. 5. Proton–proton differential elastic scattering cross sections $d\sigma/d|t|$ versus $|t|$: (a) at $\sqrt{s} = 23.5$ GeV obtained with 1 200 000 events; (b) at $\sqrt{s} = 30.6$ GeV obtained with 2 900 000 events; (c) at $\sqrt{s} = 52.8$ GeV obtained with 2 700 000 events; (d) at $\sqrt{s} = 62.3$ GeV obtained with 1 400 000 events. The curves correspond to the fit discussed in the text.

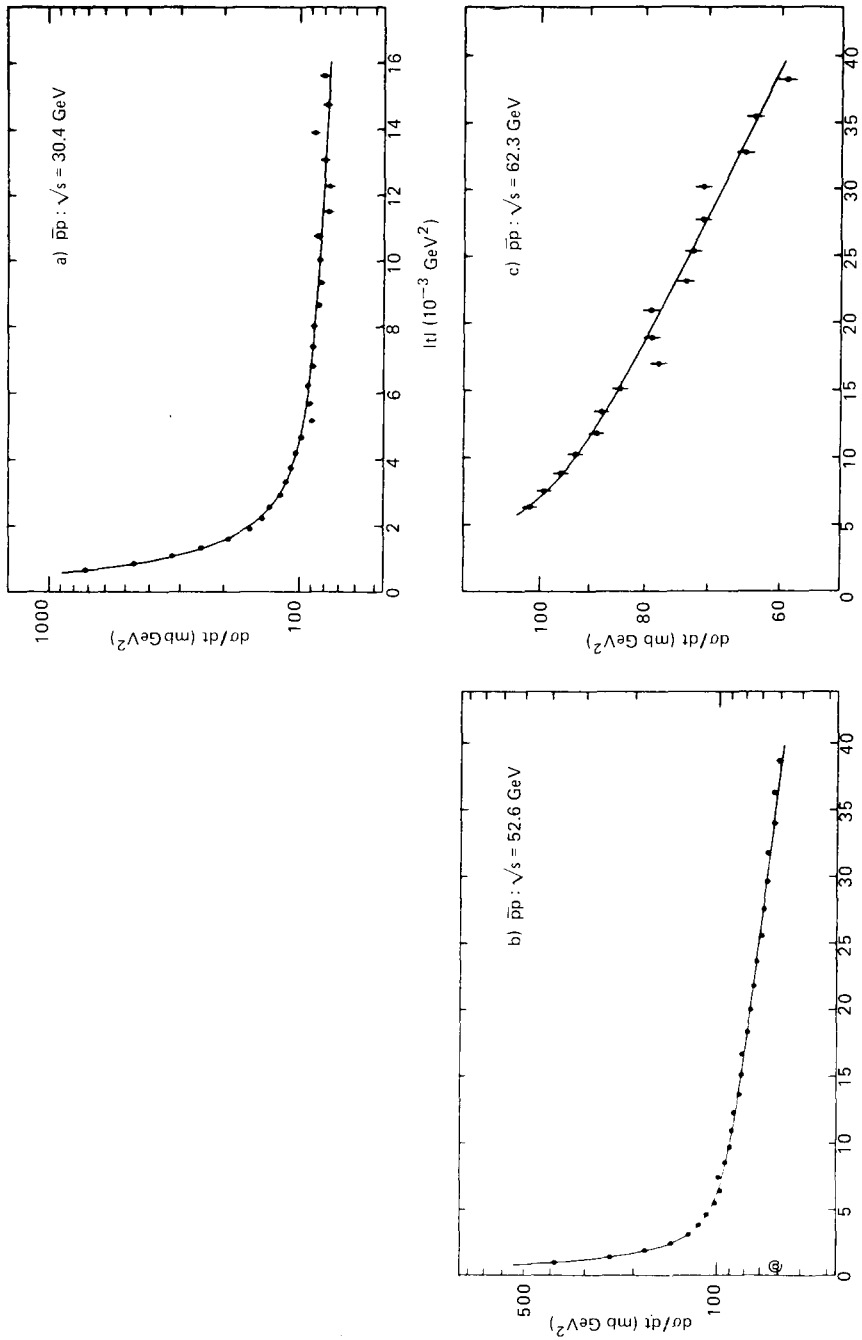

Fig. 6. Antiproton–proton differential elastic cross sections $d\sigma/d|t|$ versus $|t|$: (a) at $\sqrt{s}$ = 30.4 GeV obtained with 59 000 events; (b) at $\sqrt{s}$ = 52.6 GeV obtained with 170 000 events; (c) at $\sqrt{s}$ = 62.3 GeV obtained with 120 000 events. The curves correspond to the fit discussed in the text.

TABLE 2

Measured differential elastic cross sections

$\|t\|$ 10^{-3} (GeV^2)	$d\sigma/dt$ (mb/GeV^2)	$\|t\|$ 10^{-3} (GeV^2)	$d\sigma/dt$ (mb/GeV^2)	$\|t\|$ 10^{-3} (GeV^2)	$d\sigma/dt$ (mb/GeV^2)	$\|t\|$ 10^{-3} (GeV^2)	$d\sigma/dt$ (mb/GeV^2)
pp: $\sqrt{s}$ = 23.5 GeV		8.11	77.0 ± 2.3	8.76	75.2 ± 0.3	12.69	77.9 ± 0.3
		8.61	71.5 ± 2.2	9.43	75.5 ± 0.3	14.11	76.8 ± 0.3
0.37	1933.8 ± 7.0	9.12	75.3 ± 2.2	10.14	73.4 ± 0.4	15.60	75.6 ± 0.3
0.48	1169.4 ± 3.2	9.65	73.3 ± 2.2	10.87	72.2 ± 0.4	17.18	73.6 ± 0.3
0.61	753.2 ± 2.2	10.20	73.0 ± 2.2	11.62	72.3 ± 0.4	18.83	71.8 ± 0.3
0.75	518.9 ± 1.5			12.40	71.5 ± 0.4	20.55	70.1 ± 0.3
0.91	375.8 ± 1.6	pp: $\sqrt{s}$ = 30.6 GeV		13.20	70.8 ± 0.4	22.35	68.4 ± 0.3
1.08	289.0 ± 1.4			14.03	69.5 ± 0.4	24.22	67.3 ± 0.3
1.26	227.4 ± 1.2	0.50	1059.5 ± 2.5	14.89	69.7 ± 0.4	26.17	65.4 ± 0.3
1.47	188.4 ± 1.1	0.68	620.1 ± 1.3	15.77	68.2 ± 0.4	28.20	63.0 ± 0.4
1.68	161.6 ± 1.0	0.87	396.7 ± 1.0	16.67	68.1 ± 0.4	30.30	61.8 ± 0.4
1.91	142.7 ± 1.0	1.10	278.7 ± 0.9	17.60	67.0 ± 0.4	32.47	59.8 ± 0.4
2.16	128.1 ± 0.9	1.35	208.9 ± 0.7			34.73	57.8 ± 0.4
2.42	117.2 ± 0.8	1.62	167.9 ± 0.7	pp: $\sqrt{s}$ = 52.8 GeV		37.05	55.8 ± 0.3
2.70	107.3 ± 0.8	1.92	141.1 ± 0.6			39.46	55.1 ± 0.3
2.99	101.6 ± 0.8	2.24	124.0 ± 0.6	1.07	283.1 ± 1.0	41.93	53.5 ± 0.3
3.29	96.6 ± 0.8	2.59	111.1 ± 0.6	1.51	181.9 ± 0.6	44.49	51.4 ± 0.3
3.61	93.9 ± 0.8	2.97	102.8 ± 0.5	2.03	137.2 ± 0.5	47.12	50.8 ± 0.3
3.95	89.3 ± 0.7	3.37	98.2 ± 0.4	2.62	114.9 ± 0.4	49.82	49.1 ± 0.3
4.30	86.2 ± 0.7	3.79	92.6 ± 0.3	3.29	103.4 ± 0.4	52.60	47.4 ± 0.3
4.66	85.5 ± 0.7	4.24	88.6 ± 0.3	4.03	96.2 ± 0.3	55.46	46.0 ± 0.3
5.04	83.2 ± 0.7	4.72	86.4 ± 0.3	4.85	91.8 ± 0.4		
5.43	81.3 ± 0.7	5.22	83.2 ± 0.3	5.74	88.1 ± 0.4	pp: $\sqrt{s}$ = 62.3 GeV	
5.84	81.4 ± 0.7	5.74	81.3 ± 0.3	6.71	86.4 ± 0.4		
6.27	79.4 ± 1.0	6.30	80.5 ± 0.3	7.75	84.4 ± 0.4	5.43	94.7 ± 0.8
6.71	78.8 ± 2.3	6.87	78.3 ± 0.3	8.87	82.8 ± 0.4	6.56	91.1 ± 0.5
7.16	79.9 ± 2.3	7.48	77.2 ± 0.3	10.07	81.1 ± 0.4	7.79	88.2 ± 0.6
7.63	75.5 ± 2.3	8.10	76.2 ± 0.3	11.34	79.8 ± 0.3	9.12	87.0 ± 0.6

with $\Delta\sigma_{tot} = \sigma_{tot}(\bar{p}p) - \sigma_{tot}(pp)$. We find* $b(\bar{p}p) = 12.7$ GeV^{-2}. This can be compared to a recent fit of the pp and $\bar{p}p$ forward hadronic slopes which predicts: $b(\bar{p}p) = 12.6$ GeV^{-2} at $\sqrt{s} = 30.4$ GeV [20]. We allow for an error of 0.5 GeV^{-2} on this estimate.

The ρ-value is a free parameter at all energies except for $\bar{p}p$ and pp at $\sqrt{s} = 62.3$ GeV, where data points in the Coulomb-hadronic interference region were omitted to minimize the sensitivity to trigger counter efficiency corrections (see sect. 6). Here the previous measurement of $\rho(pp)$ and the dispersion-relation prediction for $\rho(\bar{p}p)$ [4] are used as input to a fit with σ_{tot} and b as free parameters.

The results of these fits are given in table 4. The curves in figs. 5 and 6 represent the best fit to the data.

The statistical error and the errors induced by the uncertainties in the input parameters, the normalization of the data and the t-scale calibration are given in

* With the ratio $\sigma_{el}(\bar{p}p)/\sigma_{tot}(\bar{p}p) \approx 0.17$ as for pp at ISR energies [21], $\Delta\sigma_{tot} = 48.4(E_{lab})^{-0.55} = 1.6$ mb [4] and $b(pp) = 12.2$ GeV^{-2} [19].

TABLE 3

Measured differential elastic cross sections (continued)

$\|t\|$ 10^{-3} (GeV^2)	$d\sigma/dt$ (mb/GeV^2)	$\|t\|$ 10^{-3} (GeV^2)	$d\sigma/dt$ (mb/GeV^2)	$\|t\|$ 10^{-3} (GeV^2)	$d\sigma/dt$ (mb/GeV^2)	$\|t\|$ 10^{-3} (GeV^2)	$d\sigma/dt$ (mb/GeV^2)
pp: $\sqrt{s}=62.3$ GeV		1.33	247.1 ± 4.5	$\bar{p}p$: $\sqrt{s}=52.6$ GeV		31.77	66.1 ± 1.8
		1.60	192.4 ± 4.8			33.99	62.8 ± 1.7
10.56	84.4 ± 0.6	1.89	156.9 ± 4.4	0.97	386.5 ± 9.0	36.28	62.8 ± 1.7
12.11	82.2 ± 0.6	2.21	140.4 ± 4.1	1.39	242.8 ± 2.9	38.66	60.3 ± 1.7
13.76	80.8 ± 0.4	2.56	131.1 ± 3.1	1.89	181.9 ± 1.9		
15.52	79.1 ± 0.4	2.93	118.8 ± 2.9	2.46	146.8 ± 2.1	$\bar{p}p$: $\sqrt{s}=62.3$ GeV	
17.38	77.1 ± 0.4	3.32	113.4 ± 2.8	3.10	127.3 ± 1.9		
19.35	75.7 ± 0.4	3.74	108.2 ± 2.8	3.82	116.3 ± 1.8	6.32	102.4 ± 1.6
21.43	72.4 ± 0.4	4.19	103.4 ± 2.7	4.62	109.1 ± 1.6	7.52	99.5 ± 1.6
23.61	71.2 ± 0.4	4.66	98.6 ± 2.6	5.49	101.7 ± 1.4	8.83	96.0 ± 1.6
25.89	68.8 ± 0.3	5.16	89.6 ± 2.5	6.43	97.4 ± 1.3	10.25	93.0 ± 1.5
28.29	67.6 ± 0.3	5.68	91.4 ± 2.5	7.45	98.8 ± 1.3	11.77	88.9 ± 1.5
30.78	64.7 ± 0.3	6.22	92.7 ± 2.6	8.55	93.3 ± 1.3	13.39	88.1 ± 1.5
33.39	62.2 ± 0.3	6.80	88.6 ± 2.5	9.72	90.0 ± 1.3	15.12	84.5 ± 1.5
36.09	60.9 ± 0.3	7.39	88.8 ± 2.5	10.97	88.7 ± 1.3	16.96	78.2 ± 1.4
38.91	58.3 ± 0.4	8.01	87.7 ± 2.5	12.29	87.4 ± 1.3	18.90	79.2 ± 1.4
41.83	55.9 ± 0.4	8.66	83.9 ± 2.4	13.68	83.2 ± 1.2	20.95	79.1 ± 1.4
44.85	54.8 ± 0.4	9.33	82.4 ± 2.4	15.15	81.9 ± 1.2	23.10	73.7 ± 1.4
47.98	52.9 ± 0.4	10.03	83.6 ± 2.4	16.70	81.9 ± 1.2	25.35	72.5 ± 1.4
51.22	49.4 ± 0.4	10.75	84.7 ± 3.8	18.32	78.1 ± 1.2	27.71	70.9 ± 1.3
		11.50	77.0 ± 3.6	20.01	76.0 ± 1.2	30.18	71.1 ± 1.3
$\bar{p}p$: $\sqrt{s}=30.4$ GeV		12.27	76.6 ± 3.6	21.79	74.1 ± 1.2	32.75	65.0 ± 1.3
		13.07	79.5 ± 3.7	23.63	72.4 ± 1.1	35.43	63.7 ± 1.3
0.67	718.6 ± 12.6	13.89	87.2 ± 3.9	25.55	69.4 ± 1.1	38.21	59.4 ± 1.2
0.86	460.6 ± 7.2	14.73	78.1 ± 3.7	27.55	68.4 ± 1.3		
1.08	323.5 ± 6.0	15.61	80.2 ± 3.7	29.62	66.4 ± 1.8		

table 5. Added in quadrature they yield the errors quoted in table 4. The uncertainties in the trigger counter efficiency corrections are folded into the errors on the results of pp and $\bar{p}p$ at $\sqrt{s}=62.3$ GeV. The results were hardly affected by the uncertainties in the diamond shape, diamond position, detector geometry and beam momentum.

Systematic errors stem from a possible under-estimation of efficiencies by 0.2%, an uncertainty of 0.3% (0.1%) in the stack (finger) size and an eventual loss of events between counters (<0.1%). When added in quadrature, this corresponds to a scale error of 0.4% in the normalization of the data. This scale error contributes <0.09 mb to the total cross-section, <0.004 to the ρ-value and <0.03 GeV^{-2} to the hadronic slope parameter (see table 5).

The pp data at $\sqrt{s}=23.5$, 30.6 and 52.8 were taken in two ISR runs each and results obtained from these runs individually were found to be consistent.

In fig. 7 the quantity $(d\sigma/dt)/(d\sigma/dt)_{\rho=0}-1$ is plotted against four-momentum transfer for the pp and $\bar{p}p$ data from which ρ-values were extracted. The destructive (constructive) interference in pp ($\bar{p}p$) scattering at ISR energies is evident.

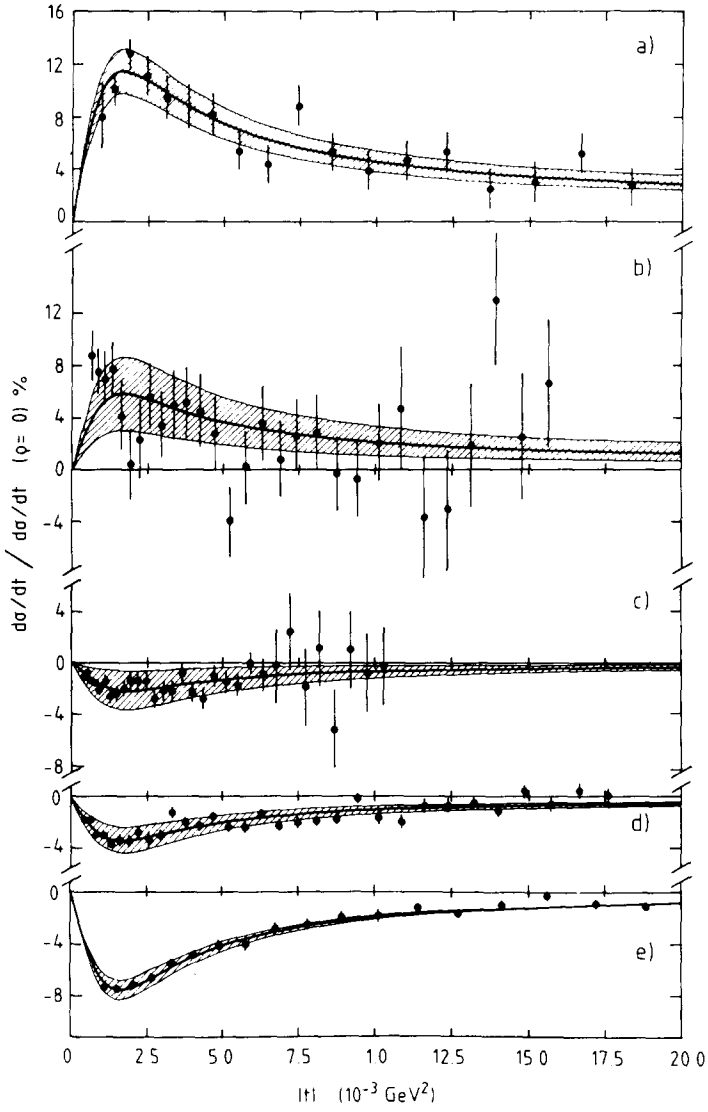

Fig. 7. The quantity $(d\sigma/dt)/(d\sigma/dt)_{\rho=0} - 1$ versus $|t|$: (a) $\bar{p}p$ at $\sqrt{s} = 52.6$ GeV; (b) $\bar{p}p$ at $\sqrt{s} = 30.4$ GeV; (c) pp at $\sqrt{s} = 23.5$ GeV; (d) pp at $\sqrt{s} = 30.6$ GeV; (e) pp at $\sqrt{s} = 52.8$ GeV. The curves represent the fit discussed in the text. The shaded area corresponds to the uncertainty in the ρ-value.

The total elastic cross sections and the ratio σ_{el}/σ_{tot} are given in table 6. They are calculated using eq. (8) where it is assumed that the differential elastic cross section falls off exponentially with $|t|$. We did not venture upon a numerical integration of the $d\sigma/d|t|$-distributions out to large values of $|t|$ [21], but estimate that the approximation used here yields results on $\sigma_{el}(pp)$ which are about 4% lower than

TABLE 4

Resulting values for σ_{tot}, ρ and b

	$\sqrt{s}$ (GeV)	δh (mm)	σ_{tot} (mb)	ρ	b (GeV^{-2})	χ^2/df
pp	23.5	-0.19 ± 0.03	39.65 ± 0.22	0.022 ± 0.014	$(11.80 \pm 0.30)^{(i)}$	1.03
pp	30.6	-0.11 ± 0.02	40.11 ± 0.17	0.034 ± 0.008	$(12.20 \pm 0.30)^{(i)}$	1.40
$\bar{p}p$	30.4	(-0.11 ± 0.02)	42.13 ± 0.57	0.055 ± 0.029	$(12.70 \pm 0.50)^{(ii)}$	1.15
$\bar{p}p - pp$			2.02 ± 0.60	0.021 ± 0.030		
pp	52.8	(-0.19 ± 0.03)	42.38 ± 0.15	0.077 ± 0.009	$12.87 \pm 0.14^{(a)}$	1.43
$\bar{p}p$	52.6	(-0.19 ± 0.03)	43.32 ± 0.34	0.106 ± 0.016	$13.03 \pm 0.52^{(b)}$	0.97
$\bar{p}p - pp$			0.94 ± 0.37	0.029 ± 0.018	0.16 ± 0.54	
pp	62.3	(-0.11 ± 0.02)	43.55 ± 0.31	$(0.095 \pm 0.011)^{(iii)}$	$13.02 \pm 0.27^{(c)}$	1.32
$\bar{p}p$	62.3	(-0.11 ± 0.02)	44.12 ± 0.39	$(0.104 \pm 0.011)^{(iv)}$	$13.47 \pm 0.52^{(d)}$	1.02
$\bar{p}p - pp$			0.57 ± 0.50		0.45 ± 0.59	

Input to the fits are given in brackets: (i) ref. [19], (ii) extrapolation explained in the text, (iii) ref. [4], (iv) dispersion-relation prediction [4]. (a) $0.001 < |t| < 0.056$, (b) $0.001 < |t| < 0.039$, (c) $0.005 < |t| < 0.052$, (d) $0.006 < |t| < 0.038$ GeV^2

TABLE 5

Error contributions

		$\sqrt{s}$ (GeV)	Stat	Norm	$\|t\|$-scale	ρ	b	Total error	Scale error	
σ_{tot}	pp	23.5	0.10	0.11	0.16		0.04	0.22	0.06	(mb)
ρ			0.004	0.006	0.009		0.007	0.014	0.002	
σ_{tot}	pp	30.6	0.03	0.13	0.07		0.08	0.17	0.08	(mb)
ρ			0.003	0.002	0.007		0.003	0.008	0.001	
σ_{tot}	$\bar{p}p$	30.4	0.38	0.38	0.09		0.10	0.57	0.09	(mb)
ρ			0.024	0.011	0.005		0.003	0.029	0.000	
σ_{tot}	pp	52.8	0.04	0.13	0.05			0.15	0.07	(mb)
ρ			0.002	0.004	0.009			0.009	0.002	
b			0.09	0.04	0.09			0.14	0.02	(GeV^{-2})
σ_{tot}	$\bar{p}p$	52.6	0.29	0.12	0.14			0.34	0.05	(mb)
ρ			0.011	0.007	0.009			0.016	0.003	
b			0.49	0.09	0.14			0.52	0.03	(GeV^{-2})
σ_{tot}	pp	62.3	0.06	0.30	0.02	0.05		0.31	0.09	(mb)
b			0.10	0.23	0.03	0.09		0.27	0.00	(GeV^{-2})
σ_{tot}	$\bar{p}p$	62.3	0.22	0.28	0.02	0.16		0.39	0.09	(mb)
b			0.46	0.19	0.00	0.12		0.52	0.01	(GeV^{-2})

TABLE 6

Total elastic cross sections

	$\sqrt{s}$ (GeV)	σ_{el} (mb)	σ_{el}/σ_{tot}
pp	23.5	6.81 ± 0.19	0.172 ± 0.005
pp	30.6	6.75 ± 0.17	0.168 ± 0.004
pp	52.8	7.17 ± 0.09	0.169 ± 0.002
pp	62.3	7.51 ± 0.19	0.172 ± 0.004
$\bar{p}p$	30.4	7.16 ± 0.34	0.170 ± 0.007
$\bar{p}p$	52.6	7.44 ± 0.32	0.172 ± 0.007
$\bar{p}p$	62.3	7.46 ± 0.32	0.169 ± 0.007

a numerical integration would give. One may assume the systematic error on $\sigma_{el}(\bar{p}p)$ to be about the same.

8. Discussion

A survey of results on $\sigma_{tot}(pp)$ and $\sigma_{tot}(\bar{p}p)$ in the ISR energy range is shown in fig. 8. Our measurement of $\sigma_{tot}(pp)$ at $\sqrt{s} = 23.5$ GeV is in agreement with the FNAL results of Carroll et al. [22] but previous ISR results are systematically lower by about 0.7 mb. At higher energies, the agreement between the various ISR measurements of $\sigma_{tot}(pp)$ is good, as can be judged from the compilation presented in table 7. The average of the ISR results is also updated in this table.

It is apparent from fig. 8 that $\sigma_{tot}(\bar{p}p)$ is rising through the ISR energy range. The magnitude of this rise is 1.99 ± 0.69 mb from $\sqrt{s} = 30.6$ to 62.3 GeV, in agreement with the rise of 2.34 ± 0.64 mb observed by Carboni et al. [23]. However, the values reported by these authors for $\sigma_{tot}(\bar{p}p)$ are higher than ours by about 1 mb.

Our measurements of $\rho(pp)$ are shown in fig. 9 together with other measurements in the ISR energy range. The agreement between the experiments is very good and

TABLE 7

Compilation of ISR results on $\sigma_{tot}(pp)$ (mb)

Ref.	$\sqrt{s} = 23.5$	30.7	44.7	52.8	62.5 GeV
[33]	38.70 ± 0.70	40.00 ± 0.60	42.50 ± 0.80	42.90 ± 0.70	44.10 ± 0.90
[34]	39.10 ± 0.30	40.10 ± 0.30	42.00 ± 0.30	42.90 ± 0.30	43.70 ± 0.40
[35]	38.89 ± 0.21	40.17 ± 0.21	41.66 ± 0.19	42.46 ± 0.26	43.04 ± 0.29
[23]		40.22 ± 0.21		43.01 ± 0.27	43.82 ± 0.30
This exp.	39.65 ± 0.22	40.11 ± 0.17		42.38 ± 0.15	43.55 ± 0.31
Average	39.20 ± 0.13	40.14 ± 0.10	41.79 ± 0.16	42.57 ± 0.11	43.51 ± 0.16
χ^2/df	2.33	0.06	0.21	1.47	1.09

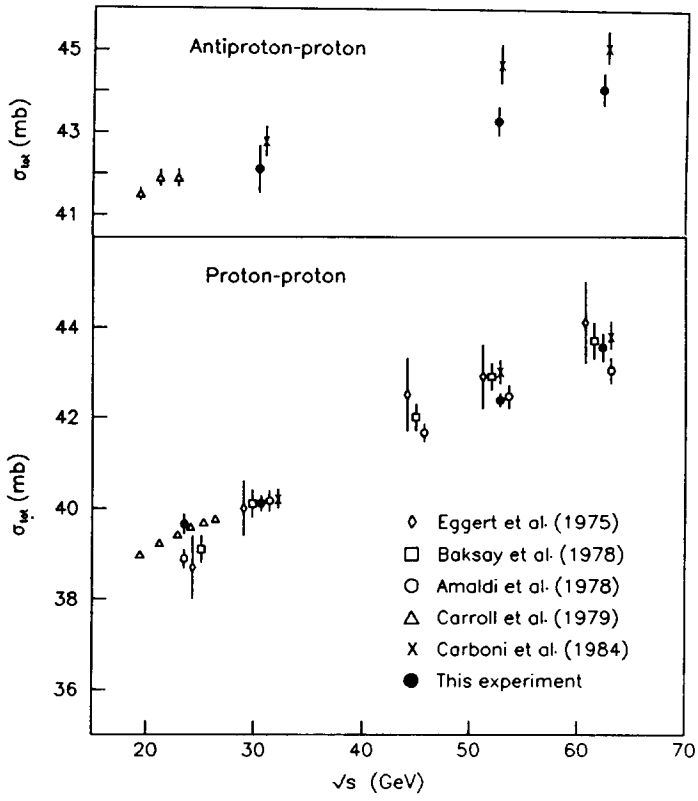

Fig. 8. Compilation of pp and $\bar{p}p$ total cross sections in the ISR energy range [22, 23, 33, 34, 35].

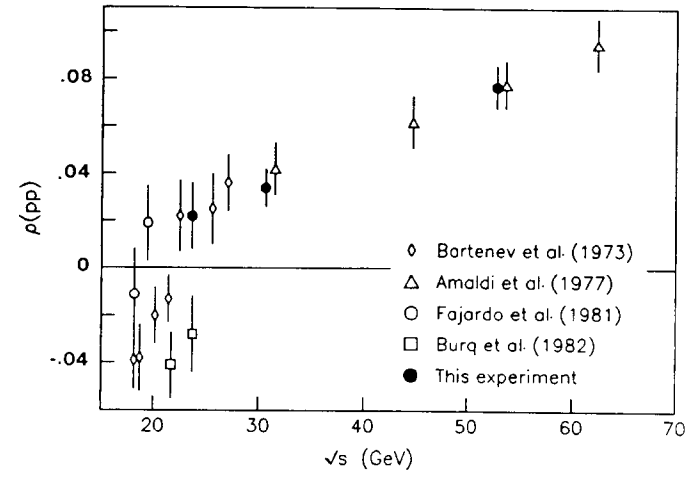

Fig. 9. Compilation of data on ρ(pp) in the ISR energy range [4, 25, 38].

TABLE 8

Compilation of ISR results on ρ(pp)

Ref.	$\sqrt{s}=23.5$	30.7	44.7	52.8	62.5 GeV
[3]	0.02 ± 0.05	0.03 ± 0.06			
[4]		0.042 ± 0.011	0.062 ± 0.011	0.078 ± 0.010	0.095 ± 0.011
This exp.	0.022 ± 0.014	0.034 ± 0.008		0.077 ± 0.009	
Average	0.022 ± 0.013	0.037 ± 0.006	0.062 ± 0.011	0.077 ± 0.007	0.095 ± 0.011

ISR averages of ρ(pp) are given in table 8. The measured values for $\rho(\bar{p}p)$ are significantly positive indicating that the observed rise of the $\bar{p}p$ total cross section will persist at higher energies. This has been recently confirmed by measurements performed at the SPS Collider [7, 8].

We have fitted the pp and $\bar{p}p$ data on ρ and σ_{tot} using dispersion relations. The fixed-t dispersion relation connecting the energy dependence of the real and the imaginary part of the forward scattering amplitude can be approximated at ISR energies by the principal value integral [4]:

$$\rho_{\pm}(E)\sigma_{\pm}(E)=\frac{C}{p}+\frac{E}{\pi p}\int_{m}^{\infty}\mathrm{d}E'\,p'\left\{\frac{\sigma_{\pm}(E')}{E'(E'-E)}-\frac{\sigma_{\mp}(E')}{E'(E'+E)}\right\}. \tag{14}$$

Here m is the proton mass, p the laboratory momentum, E the laboratory energy and C an integration constant. The subscripts (+) and (−) refer to pp and $\bar{p}p$ respectively.

As in ref. [4], the energy dependence of the total cross section was parametrized as:

$$\sigma_{\pm}=C_0+C_1(E/E_0)^{-\alpha_1}\mp C_2(E/E_0)^{-\alpha_2}+C_3[\ln(s/s_0)]^{\gamma}\ (\mathrm{mb}), \tag{15}$$

with the scale factor E_0 (s_0) arbitrarily fixed to 1 GeV (1 GeV^2). We fitted 142 data points measured at $E>10$ GeV [24] and the minimization resulted in a $\chi^2/\mathrm{d}f=1.15$. Not included were the measurements of ρ(pp) by Fajardo et al. [25] and of $\sigma_{tot}(\bar{p}p)$ by Carboni et al. [23]. The former are in disagreement with a body of data on ρ(pp) at $\sqrt{s}\approx 15$ GeV while the latter are inconsistent with our measurements. The fitted values of the parameters are listed in table 9 and the resulting curves are shown in figs. 10 and 11. The fitted values of σ_{tot} and ρ at ISR and SPS Collider energies are given in table 10.

TABLE 9

Results of the dispersion-relation fit

$C=-30.0\pm3.8$	$C_0=28.3\pm0.2$
$C_1=43.0\pm0.6$	$\alpha_1=0.41\pm0.01$
$C_2=24.8\pm0.9$	$\alpha_2=0.56\pm0.01$
$C_3=0.19\pm0.01$	$\gamma=2.02\pm0.01$

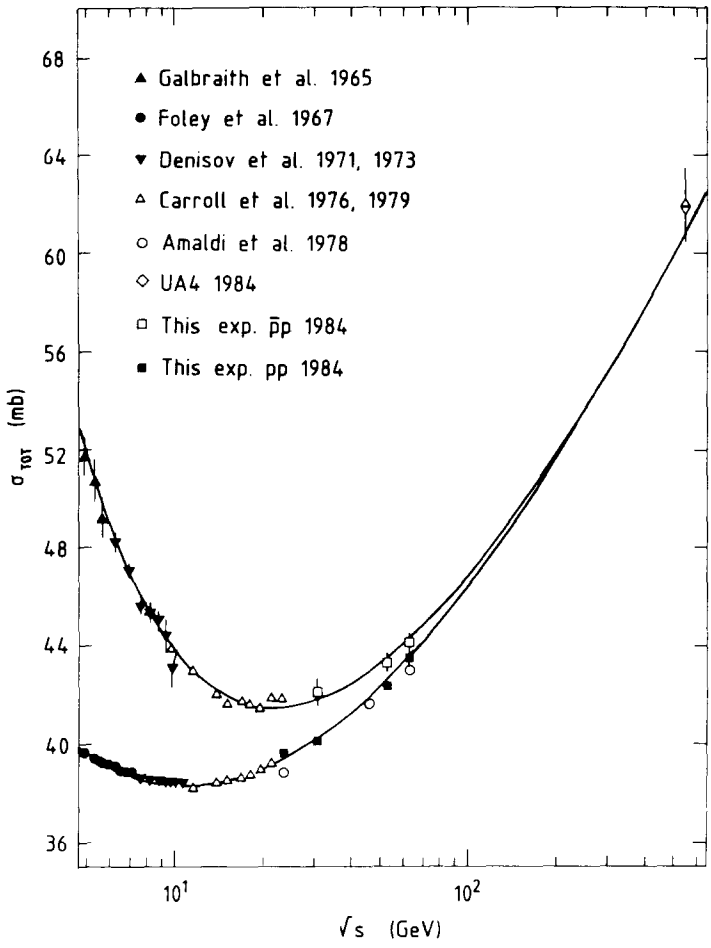

Fig. 10. Summary of high-energy data on $\sigma_{tot}(pp)$ and $\sigma_{tot}(\bar{p}p)$ [8, 22, 31, 32, 35, 37]. The curve corresponds to the dispersion-relation fit described in the text. Not all data points used in the fit are shown.

TABLE 10

Fitted values of σ_{tot} and ρ at various energies

$\sqrt{s}$ (GeV)	$\sigma_{tot}(pp)$ (mb)	$\sigma_{tot}(\bar{p}p)$ (mb)	$\rho(pp)$	$\rho(\bar{p}p)$
23.5	39.45 ± 0.01	41.54 ± 0.04	0.002 ± 0.001	0.043 ± 0.001
30.7	40.31 ± 0.02	41.85 ± 0.04	0.031 ± 0.001	0.060 ± 0.001
44.7	41.86 ± 0.04	42.88 ± 0.05	0.061 ± 0.001	0.079 ± 0.001
52.8	42.68 ± 0.05	43.52 ± 0.06	0.072 ± 0.002	0.087 ± 0.002
62.5	43.58 ± 0.07	44.27 ± 0.07	0.082 ± 0.002	0.093 ± 0.002
550	60.82 ± 0.40	60.88 ± 0.40	0.129 ± 0.002	0.129 ± 0.002

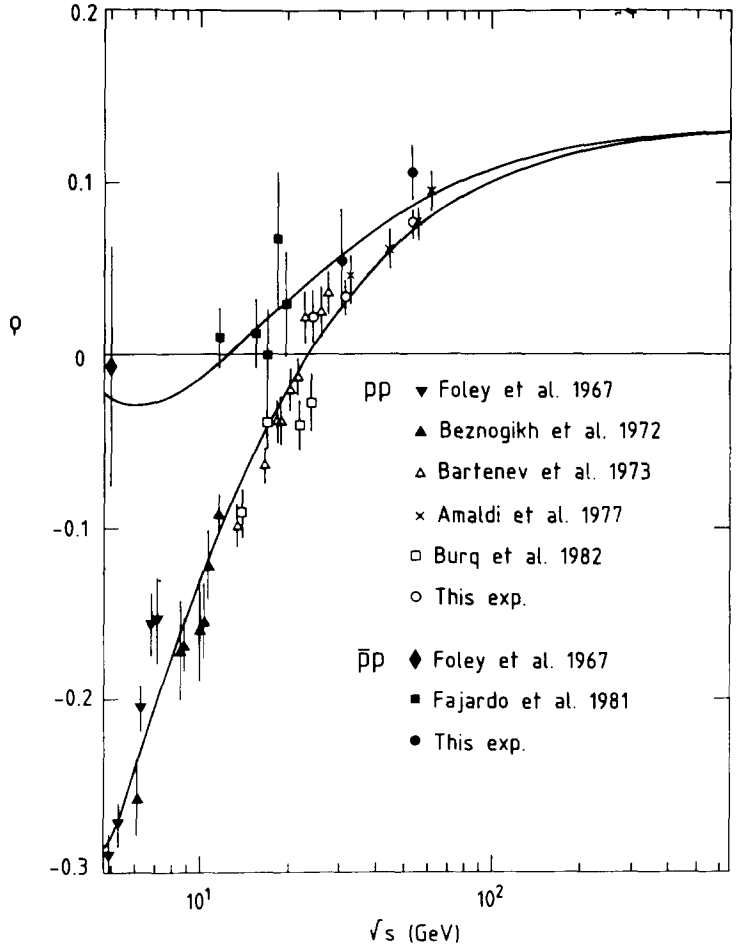

Fig. 11. Compilation of pp and $\bar{p}p$ ρ-values [4, 25, 37, 38]. Not shown are an early measurement of Amaldi et al. [3] and pp data of Fajardo et al. [25]. The curve corresponds to the dispersion-relation fit described in the text.

It is seen from eq. (7) that the theoretical uncertainty in the calculation of the Coulomb-hadronic phase induces a systematic error in the determination of the ρ-values. We estimated this uncertainty by allowing data points of $\rho(pp)$ and $\rho(\bar{p}p)$ to float in opposite directions by an amount $\Delta\alpha\phi$ constrained to lie within the systematic error given by West and Yennie, $|\Delta\alpha\phi| \leq 0.015$, and found this error to be negligible: $|\Delta\alpha\phi| = 0.001 \pm 0.002$.

The results given above essentially reproduce those obtained by Amaldi et al. [4]. In particular, the Froissart bound [26] is found to be qualitatively saturated: $\gamma = 2$. The parametrization (15) gives a very good description of the energy dependence of σ_{tot}, and of ρ through eq. (14), up to SPS Collider energies.

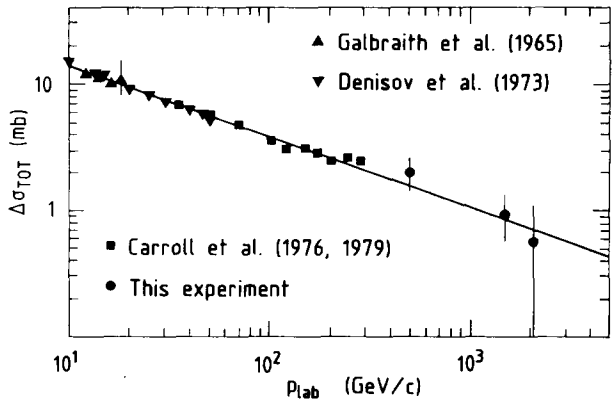

Fig. 12. The difference $\Delta\sigma_{tot} = \sigma_{tot}(\bar{p}p) - \sigma_{tot}(pp)$ versus laboratory momentum p_{lab} [22, 31, 32]. The curve corresponds to the dispersion-relation fit described in the text.

The energy dependence of the cross-section difference, $\Delta\sigma_{tot} = \sigma_{tot}(\bar{p}p) - \sigma_{tot}(pp)$, is shown in fig. 12. The line represents the result of the dispersion-relation fit discussed above. The data follow a power law fall-off over a large range in laboratory energy, $10 < E < 2000$ GeV, in accordance with Regge exchange of the dominant odd-signature trajectories ρ and ω.

A vanishing cross section difference is a sufficient, but not a necessary, condition to satisfy the present version of the Pomeranchuck theorem. This theorem states that if one of the cross sections $\sigma_{tot}(pp)$ or $\sigma_{tot}(\bar{p}p)$ continues to increase with increasing energy, then their ratio $\sigma_{tot}(\bar{p}p)/\sigma_{tot}(pp) \to 1$ at very high energies. Several authors [27-29] have commented on the existence of odd-signature contributions to the scattering amplitude ("odderons") which are admitted by the theorem and which would cause $\Delta\sigma_{tot}$ to approach a constant or even increase like $\ln(s)$ with energy. Such unconventional contributions are restricted by the measurements of this experiment. Block and Cahn [27], for instance, have concluded on the basis of fits of pp and $\bar{p}p$ total cross sections and ρ-values to various analytic scattering amplitudes that the strength of the odderon amplitude, if it exists at all, should be less than 1% of the dominant even-signature amplitude.

Our measurements of $b(pp)$ and $b(\bar{p}p)$ indicate that both are rising with energy and that they are not significantly different at ISR energies. This is in accordance with the theorem of Cornille and Martin [30], which predicts that the ratio of the widths of the diffraction peaks will approach unity at very high energies.

We are indebted to the CERN-Rome Collaboration for making available to us part of the equipment they used and to the CERN-Naples-Pisa-Stony Brook Collaboration for providing us with signals of their detector. P. Macq and J.C. Sens are acknowledged for their contributions at the early stage of the experiment. We further thank the technical staffs of the Louvain and Northwestern Universities and the CERN ISR, EP and DD Divisions for their support. We gratefully acknowledge

the contribution to this experiment of the late J. Debaisieux who designed most of the on-line monitoring programs.

This work was supported in part by the Institut Interuniversitaire des Sciences Nucleaires, Belgium, and in part by a US Department of Energy grant.

References

[1] U. Amaldi et al., Phys. Lett. 44B (1973) 112
[2] S.R. Amendolia et al., Phys. Lett. 44B (1973) 119; Nuovo Cim. 17A (1973) 735
[3] U. Amaldi et al., Phys. Lett. 43B (1973) 231
[4] U. Amaldi et al., Phys. Lett. 66B (1977) 390
[5] N. Amos et al., Phys. Lett. 120B (1983) 460; 128B (1983) 343
[6] G. Carboni et al., Phys. Lett. 108B (1982) 145; 113B (1982) 87;
M. Ambrosio et al., Phys. Lett. 115B (1982) 495
[7] G. Arnison et al., Phys. Lett., 121B (1983) 77
[8] M. Bozzo et al., Phys. Lett. B147 (1984) 392
[9] H.A. Bethe, Ann. of Phys. 3 (1958) 190
[10] G.B. West and D.R. Yennie, Phys. Rev. 172 (1968) 1413
[11] R. Cahn, Z. Phys. C15 (1982) 253
[12] P.S. Staff, IEEE Trans. Nucl. Sci. NS-30 No. 4 (1983) 2039
[13] P.J. Bryant, IEEE Trans. Nucl. Sci. NS-30 No. 4 (1983) 2047
[14] K.M. Terwilliger, Proc. Int. Conf. on High-energy accelerators (CERN, Geneva, 1959) 53
[15] S. Van der Meer, CERN Internal Report ISR-PO/68-31 (1968)
[16] P. Bryant and K. Potter, CERN internal report ISR/ES/BOM/82-15 (1982)
[17] N. Amos, Ph.D. thesis, Northwestern University (1985) unpublished;
M. Botje, Ph.D. thesis, State University Utrecht (1984) unpublished;
J-P. Matheys, Ph.D. thesis, Université Catholique de Louvain (1984), unpublished
[18] N. Amos et al., North-Western University Internal Report 101 (1981)
[19] CERN-Pisa-Rome-Stony Brook Collaboration, Phys. Lett. 62B (1976) 460
[20] M.M. Block and R.N. Cahn, Phys. Lett. 120B (1983) 229
[21] U. Amaldi and K.R. Schubert, Nucl. Phys. B166 (1980) 301
[22] A. Carroll et al., Phys. Rev. Lett. 33 (1974) 928; Phys. Lett. 61B (1976) 303; 80B (1979) 423.
[23] G. Carboni et al., Nucl. Phys. B254 (1985) 697
[24] Data on $\sigma_{tot}(pp)$: refs. [22], [23], [31], [32], [33], [34], [35], [36], [37];
Data on $\sigma_{tot}(\bar{p}p)$: refs. [8], [22], [31], [32];
Data on $\rho(pp)$: refs. [4], [37], [38];
Data on $\rho(\bar{p}p)$: refs. [25], [37]
[25] L. Fajardo et al., Phys. Rev. Lett. D24 (1981) 46
[26] M. Froissart, Phys. Rev. B123 (1961) 1053;
A. Martin, Nuovo Cim. 42 (1966) 930
[27] M.M. Block and R.N. Cahn, Phys. Lett. 120B (1983) 224
[28] P. Gauron and B. Nicolescu, Phys. Lett. 124B (1983) 249
[29] A. Martin, Z. Phys. C15 (1982) 185
[30] H. Cornille and A. Martin, Phys. Lett. 40B (1972) 671
[31] W. Galbraight et al., Phys. Rev. 138 (1965) B913
[32] S. Denisov et al., Phys. Lett. 36B (1971) 415, 528;
Nucl. Phys. B65 (1973) 1
[33] K. Eggert et al., Nucl. Phys. B98 (1975) 93
[34] L. Baksay et al., Nucl. Phys. B141 (1978) 1
[35] U. Amaldi et al., Nucl. Phys. B145 (1978) 367
[36] G. Bellettini et al., Phys. Lett. 14 (1965) 164
[37] K. Foley et al., Phys. Rev. Lett. 19 (1967) 857
[38] V. Bartenev et al., Phys. Rev. Lett. 29 (1972) 1755; 31 (1973) 1088, 1367;
G. Beznogikh et al., Phys. Lett. 39B (1972) 411; 43B (1973) 85;
J.P. Burq et al., Phys. Lett. 109B (1982) 124